The Kinetics of the Nitriding of Ternary Fe-2 at pct Cr-2 at pct Ti Alloy

K.S. JUNG, R.E. SCHACHERL, E. BISCHOFF, and E.J. MITTEMEIJER

The mechanism and the kinetics of growth of the nitrided zone of ternary Fe-2 at pct Cr-2 at pct Ti alloy was investigated by performing gaseous nitriding experiments at temperatures of 833 K and 853 K (560 °C and 580 °C) and at nitriding potentials $r_N = 0.004 \text{ atm}^{-1/2}$ and $0.054 \text{ atm}^{-1/2}$. The microstructure of the nitrided zone was investigated by transmission electron microscopy and the elemental compositional variation with depth was determined by employing electron probe microanalysis. Fine platelet-type mixed $Cr_{1-x}Ti_xN$ nitride precipitates developed in the nitrided zone. To describe the evolution of the nitrogen concentration depth profile, a numerical model was developed with the following parameters: the surface nitrogen content, the solubility product(s) of the alloying elements and dissolved nitrogen in the ferrite matrix, and a parameter defining the composition of the inner nitride precipitates. These parameters were determined by fitting model-calculated nitrogen depth profiles to the corresponding experimental data. The results obtained demonstrate that the type of nitride formation (i.e., whether Cr and Ti precipitate separately, as CrN and TiN, or jointly, as mixed $Cr_{1-x}Ti_xN$) as well as the amounts of mobile and immobile excess nitrogen taken up by the specimen considerably influence the shape and extent of the nitrogen concentration profiles.

I. INTRODUCTION

NITRIDING is a thermochemical surface treatment that has been applied successfully in industry to improve properties of iron-based steel components, such as the resistances against fatigue, wear, and corrosion.[1–7] It would be beneficial to describe the kinetics of the nitriding process quantitatively to tune the resulting microstructure and thus to optimize the properties of the components. Unfortunately, current knowledge does not allow for such model-based nitriding.

So-called nitriding steels, as used in technology, usually contain more than one alloying element exhibiting a large affinity for nitrogen. As compared with a vast body of literature on the nitriding behavior of binary iron-based alloys,[8–30] only recently fundamental research on the nitriding behavior of ternary iron-based $Fe-Me_1-Me_2$ alloys has been initiated. Questions to be addressed include the following: Do Me_1 and Me_2 precipitate as separate nitrides (simultaneously or sequentially) or as mixed nitride (jointly)? Recent research on Fe-Cr-Al alloys has demonstrated that mixed nitrides can develop, metastably, a crystal structure (even) incompatible with the equilibrium crystal structure of the separate nitrides.[31] It was also shown that the ternary alloys can absorb amounts of nitrogen considerably larger than necessary for precipitation of all alloying elements as nitride and equilibrium saturation of the unstrained ferrite matrix—excess nitrogen.[32,33] Against this background, it is deemed necessary to investigate if the kinetics of the nitriding process for such alloys (1) sensitively reflects the operating mechanism of nitriding and (2) allows for the determination of physically meaningful parameters that provide a quantitative description of the nitride precipitation process. Thus not only is nitride precipitation understood but also the avenue opens up for model-based optimization of the nitrided microstructure of a multicomponent.

A quantitative description of the nitriding kinetics, as exhibited by the evolution of the nitrogen concentration depth profile, should express the roles of the diffusion of nitrogen through the matrix and the rate of precipitation of the alloying element nitrides. The shape of the nitrogen concentration depth profile depends on the strength of the interaction of the alloying elements with nitrogen and thus can be categorized as follows:

a) Strong interaction: A surface-adjacent case develops, where *all* Me atoms have precipitated. A sharp nitrided case/unnitrided core boundary occurs.
b) Weak interaction: Nitride precipitation progresses with the same rate at each depth below the surface. A nitrogen gradient is virtually absent.
c) Intermediate interaction: Depending on temperature and alloying element concentration, nitriding behavior can vary between weak and strong interaction, characterized by a diffuse nitrided case–unnitrided core boundary.

K.S. JUNG, PhD Student, and E. BISCHOFF, Senior Scientist, are with the Max Planck Institute for Intelligent Systems (formerly Max Planck Institute for Metals Research), Heisenbergstraße 3, 70569 Stuttgart, Germany. R.E. SCHACHERL, Senior Scientist, is with the Institute for Materials Science, University of Stuttgart, Heisenbergstraße 3, 70569 Stuttgart, Germany. Contact e-mail: r.schacherl@is.mpg.de E.J. MITTEMEIJER, Professor, is with the Institute for Materials Science, University of Stuttgart, and is also a Director, with the Max Planck Institute for Intelligent Systems (formerly Max Planck Institute for Metals Research).
Manuscript submitted March 14, 2011.
Article published online September 20, 2011.

Only for the extreme case of strong Me-N interaction in a binary Fe-Me alloy is the following simple analytical formulation of process kinetics possible[34]:

$$z^2 = \left(\frac{2 \times c_{N_\alpha}^s \times D_N}{n \times c_{Me}}\right) \times t \qquad [1]$$

where z is the extent of the diffusion zone (depth range below the specimen surface), $c_{N_\alpha}^s$ is the nitrogen concentration at the specimen surface, D_N is the diffusivity of the nitrogen at a given temperature, n is the stoichiometry of the MeN$_n$ precipitates, c_{Me} is the Me concentration, and t is the nitriding time.

Considering the common case of intermediate interaction, the nitriding of ternary Fe-Me$_1$-Me$_2$ alloys and the kinetic effects of excess nitrogen uptake—a much more general approach, leading to a numerical model—is required. The first attempt was presented in Reference 35; however, the calculated model results did not match the experimental data obtained. This outcome is most likely because of the possibly occurring mixed nitride formation (not considered) as well as ignorance of the role of mobile excess nitrogen. A completely different approach was presented in References 36 and 37 in which the trapping of nitrogen in Fe-Me-N configurations was proposed. This approach conflicts with the physical reality of precipitation of genuine nitride particles. The (numerical) model proposed in the present study provides a quantitative description of the nitriding kinetics of ternary Fe-Me$_1$-Me$_2$ alloys in which, for the first time, the consequences of (1) precipitation of either separate or mixed alloying element nitrides and (2) mobile and immobile excess nitrogen (Section II) taken up in the nitrided zone, can be modeled and thus investigated. The model has been applied to the nitriding of Fe-2 at pct Cr-2 at pct alloy; both Cr and Ti have a strong affinity for nitrogen. The (crystal) structure of the nitride precipitates and the microstructure of the nitrided zone were investigated by transmission electron microscopy (TEM). The nitrogen concentration depth profiles in the diffusion zone were determined by electron probe microanalysis (EPMA). The experimentally obtained nitrogen concentration depth profiles were compared with those calculated by the proposed model.

II. THEORETICAL BACKGROUND

A. Basis

In the following sections, the nitride to be precipitated is denoted as MeN$_n$, which stands for either one of the separate nitrides Me$_1$N$_n$ and Me$_2$N$_n$ or the mixed nitride (Me$_1$,Me$_2$)N$_n$ developing upon nitriding the ternary Fe-Me$_1$-Me$_2$ alloy. Previous work has shown that the total amount of nitrogen taken up by the specimen in equilibrium with the nitriding gas atmosphere, $[N]_{tot}^0$, can be subdivided in the following contributions[30–32]: (1) nitrogen incorporated in the nitride precipitates, $[N]_{MeN_n}^0$; (2) nitrogen adsorbed at the nitride–matrix interfaces, the so-called immobile excess nitrogen, $[N]_{imm,exc}^0$; and (3) nitrogen dissolved in the matrix, which is the sum of the amount of dissolved nitrogen in

pure, unstrained ferrite $[N]_\alpha^0$, and the amount of excess dissolved nitrogen resulting from the nitride–matrix misfit-strain field, the so-called mobile excess nitrogen, $[N]_{mob,exc}^0$. Thus, the following equation is true:

$$[N]_{tot}^0 = \left([N]_{MeN_n}^0 + [N]_{imm,exc}^0 + ([N]_\alpha^0 + [N]_{mob,exc}^0)\right) \qquad [2]$$

In case of an inhomogeneously nitrided specimen, the total amount of nitrogen at depth z $[N]_{tot}$ is given by an equation like Eq. [2], albeit with $[N]_{MeN_n}^0$ and $[N]_\alpha^0$ replaced by $[N]_{MeN_n}$ and $[N]_\alpha$; moreover, the amounts of immobile and mobile excess nitrogen depend on the degree of precipitation (i.e., on $[N]_{MeN_n}$) and thus depend on depth as well, and accordingly, $[N]_{imm,exc}^0$ and $[N]_{mob,exc}^0$ have to be replaced by $[N]_{imm,exc}$ and $[N]_{mob,exc}$.

Obviously, the dissolved excess nitrogen takes part in the diffusion of nitrogen through the matrix and therefore is called mobile excess nitrogen, whereas the adsorbed excess nitrogen is bonded to the nitride particles and therefore is called immobile excess nitrogen. Both types of excess nitrogen considerably influence the nitriding kinetics.

The inward diffusion of (dissolved) nitrogen in the ferrite matrix can be expressed as follows by Fick's second law:

$$\frac{\partial c_{N_\alpha}(z,t)}{\partial t} = D_N \times \frac{\partial^2 c_{N_\alpha}(z,t)}{\partial z^2} \qquad [3]$$

where $c_{N_\alpha}(z,t)$ is the (fractional) concentration of nitrogen dissolved in the ferrite matrix at depth z and time t and at a given temperature, T. D_N is the diffusion coefficient of nitrogen in the ferrite matrix, taken to be independent of nitrogen concentration (note that the values of c_{N_α} are low at <1 at pct).

The formation of nitride Me$_1$N$_n$ or nitride Me$_2$N$_n$ in the ferrite matrix can be expressed as follows:

$$Me_i + nN \Leftrightarrow Me_iN_n \qquad [4a]$$

with Me$_i$ and N as the Me$_1$ or Me$_2$ and nitrogen dissolved in the ferrite matrix. Similarly, for the formation of mixed $(Me_{1,1-x}Me_{2,x})N_n$ $(x < 1)$, nitride can be written as follows:

$$(1-x)Me_1 + xMe_2 + nN \Leftrightarrow (Me_{1,1-x}Me_{2,x})N_n \qquad [4b]$$
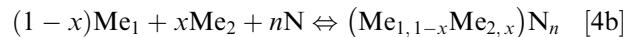
The equilibrium constants of the aforementioned reactions, K_e, are expressed as follows:

$$K_e = \frac{1}{[Me_i] \times [N]^n} = \frac{1}{K_{Me_iN_n}} \qquad [5a]$$

$$K_e = \frac{1}{[Me_1]^{1-x} \times [Me_2]^x \times [N]^n} = \frac{1}{K_{(Me_{1,1-x}Me_{2,x})N_n}} \qquad [5b]$$

where $[A]$ denotes the concentration of component A dissolved in the ferrite matrix, with $K_{Me_iN_n}$ and $K_{(Me_{1,1-x}Me_{2,x})N_n}$ as the solubility products, $K_{Me_iN_n} = [Me_i] \times [N]^n$ and $K_{(Me_{1,1-x}Me_{2,x})N_n} = [Me_1]^{1-x} \times [Me_2]^x \times$

$[N]^n$, respectively. Upon nitriding, precipitation of either separate Me_iN_n nitrides or mixed $(Me_{1,1-x}Me_{2,x})N_n$ nitride will occur at a certain location in the diffusion zone when it holds the following:

$$[Me_i] \times [N]^n > K_{Me_iN_n} \qquad [6a]$$

$$[Me_1]^{1-x} \times [Me_2]^x \times [N]^n > K_{(Me_{1,1-x}Me_{2,x})N_n} \qquad [6b]$$

B. Numerical Modeling of Nitrogen Concentration Depth Profile

The presence of immobile excess nitrogen adsorbed at the nitride–matrix interface in the present work can be taken into account by replacing the stoichiometric parameter n in the separate Me_iN_n nitrides or the mixed $(Me_{1,1-x}Me_{2,x})N_n$ nitride by $n' = n + y$ with y as the contribution of the immobile excess nitrogen (for the nitrides occurring in the nitrided Fe-based Fe-Cr-Ti alloys, it holds $n = 1$, cf. Section IV–B).

Precipitation of the alloying element nitride, at a certain location in the alloy, occurs if Eq. [6] is satisfied for the nitride considered. This can be expressed as u, which takes a value >1. For the ternary Fe-Me$_1$-Me$_2$ alloy, the following precipitation sequences can be discerned:

$$u_{Me_iN} = \frac{[Me_i] \times [N]^n}{K_{Me_iN_n}} \qquad [7a]$$

$$u_{Me_{1,1-x}Me_{2,x}N} = \frac{[Me_1]^{1-x} \times [Me_2]^x \times [N]^n}{K_{(Me_{1,1-x}Me_{2,x})N_n}} \qquad [7b]$$

First it can be assumed that the alloying elements precipitate as separate nitrides (i.e., as Me_1N_n and Me_2N_n). If one of the u values according to Eq. [7a] (i.e., either u_{CrN} or u_{TiN} in the present work) is larger than one, then, in the time step and at the location/depth considered, an amount of corresponding nitride is allowed to precipitate until the u value of this nitride equals one. If the u values according to Eq. [7a] for both alloying element nitrides (i.e., u_{CrN} and u_{TiN} in the present work) are larger than one, then, for the time step and at the location/depth considered, the amount of nitride with the highest u value is allowed to precipitate until its u value becomes smaller than the u value of the other nitride. Then, in the same time step and at the same location/depth, the other nitride is allowed to precipitate, etc. This approach is followed, in the time step and at the location/depth considered, until both u values equal one.

Second, it can be supposed that the alloying elements precipitate as a mixed $(Me_{1,1-x}Me_{2,x})N_n$ nitride. In this case, precipitation of the mixed nitride, in the time step and at the location/depth considered, occurs if $u_{(Me_{1,1-x}Me_{2,x})N_n}$ is larger than one, and with an amount leading to a reduction of $u_{(Me_{1,1-x}Me_{2,x})N_n}$ to one.

For each time step, j ($j = 0, 1, 2 \ldots$), at each location/depth considered, the amounts of Me$_1$, Me$_2$, and N remaining in solid solution, after completing the precipitations in time step j, as described previously, comply with the following:

For the precipitation of separate nitrides $Me_iN_{n'}$:

$$\left([Me_i]^{j-1} - \frac{\Delta[N]^j}{n'}\right) \times \left([N]^{j-1} - \Delta[N]^j\right) = K_{Me_iN_n} \ (j \geq 1) \qquad [8a]$$

For the precipitation of mixed nitride $(Me_{1,1-x}Me_{2,x})N_{n'}$:

$$\left([Me_1]^{j-1} - (1-x) \times \frac{\Delta[N]^j}{n'}\right)^{1-x}$$

$$\times \left([Me_2]^{j-1} - x \times \frac{\Delta[N]^j}{n'}\right)^x \times \left([N]^{j-1} - \Delta[N]^j\right)$$

$$= K_{Me_{1,1-x}Me_{2,x}N_n} \ (j \geq 1) \qquad [8b]$$

where $[Me_i]^{j-1}$ and $[N]^{j-1}$ is the amounts of dissolved Me$_i$ and N after timestep, $j - 1$ and $\Delta[N]^j$ is the amount of nitrogen taken up in $Me_iN_{n'}$ or $(Me_{1,1-x}Me_{2,x})N_{n'}$ in time step j.

The nitrogen concentration can be calculated as a function of depth and time applying a numerical finite difference (explicit) solution method for Eq. [3] as described in References 15 and 38–40. Upon executing this recursive method, at every depth for every time step, the possible precipitation of alloying element nitrides is verified and executed as described previously.

The nitrogen concentration depth profile can thus be numerically calculated based on Eqs. [3], [7], and [8] adopting values for the following parameters:

a) The amount of mobile nitrogen dissolved in the ferrite matrix at the surface of the specimen in equilibrium with the nitriding gas atmosphere, which is expressed as follows: $c_{N_\alpha}^s = [N]_\alpha^0 + [N]_{mob,exc}^0$
b) The solubility products, $K_{Me_iN_n}$, or the solubility product $K_{Me_{1-x}Me_{2x}N_n}$
c) The composition parameter: $n' = n + y$ (here with $n = 1$)

III. EXPERIMENTAL PROCEDURES

A. Sample Preparation

Ingots of Fe-2 at pct Cr-2 at pct were prepared from pure Fe (99.98 wt pct, Alfa Aesar, Ward Hill, MA), pure Cr (99.999 wt pct, Alfa Aesar), and pure Ti (99.999 wt pct, Alfa Aesar) using a light-arc furnace. The molten alloys were cast as buttons, with a shape given by a diameter of 40 mm and a height of 15 mm. The precise composition of the Fe-Ti-Cr alloys was analyzed, applying (1) inductive coupled plasma-optic emission spectroscopy to determine the content of the alloying elements Ti and Cr, (2) a combustion method to

determine the light elements C and S, and (3) a hot extraction to determine the light elements O and N. The determined composition of the alloys is shown in Table I.

The cast buttons were cold-rolled to foils with a thickness of about 1.0 mm. To reduce the rolling-induced texture of the specimen, the buttons were rolled in different directions. The foils thus obtained were cut into rectangular specimens (15×15 mm^2) and subsequently ground and polished (final stage: 1-μm diamond paste). The polished specimens were encapsulated in a quartz tube filled with Ar and annealed at 1073 K (800 °C) for 2 hours to establish a recrystallized grain structure (grain size of about 40 μm). Before nitriding, the specimens were ground and polished (last step: 1-μm diamond paste) and cleaned ultrasonically with ethanol.

B. Nitriding

For nitriding, the specimen was suspended by a quartz fiber and placed in the middle of a vertical tube furnace. The gaseous nitriding experiments were performed in a flux of an ammonia–hydrogen gas mixture (NH$_3$, >99.998 vol pct and H$_2$, 99.999 vol pct). The fluxes of both gases were precisely adjusted with mass flow controllers. The gas flow rate was kept at 500 mL/min, which, because the inner diameter of the tube furnace is 28 mm, corresponds to a linear gas velocity at room temperature of 13.5 mm/s in the furnace, which is sufficient to avoid any significant (thermal) decomposition of ammonia in the nitriding atmosphere.[41,42]

Different sets of nitriding experiments were performed at temperatures of 833 K and 853 K (560 °C and 580 °C) and at nitriding potentials of $r_N = 0.004$ atm$^{-1/2}$ and 0.054 atm$^{-1/2}$ ($r_N \equiv p_{NH_3}/p_{H_2}^{3/2}$, where p_i is the partial pressure of component i[41]), while varying the nitriding time between 1 and 24 hours. The different nitriding conditions are shown in Table II.

Under the applied nitriding conditions, no compound layer (iron nitrides: ε-Fe$_{2-3}$N and γ'-Fe$_4$N) formation occurred at the specimen surface. In the following, the different sets of nitriding conditions applied to the Fe-2 at pct Cr-2 at pct specimens: (1) at 833 K (560 °C) with $r_N = 0.054$ atm$^{-1/2}$, (2) at 833 K (560 °C) with $r_N = 0.004$ atm$^{-1/2}$, and (3) at 853 K (580 °C) with $r_N = 0.004$ atm$^{-1/2}$, which will be denoted as LTHP, LTLP, and HTLP, respectively (where L and H stand for "relatively low" and "relatively high", respectively, and T and P denote nitriding temperature and nitriding potential, respectively).

C. EPMA Analysis

The homogeneity of the distribution of the alloying elements Ti and Cr and of nitrogen in the specimens was verified by electron probe microanalysis (EPMA) using a Cameca SX100 instrument (CAMECA, Société par Actions Simplifiée (SAS), Gennevilliers Cedex, France). Pieces of the specimen were cut to prepare cross sections by subsequently embedding of these pieces with a Polyfast (Struers A/S, Ballerup, Denmark) (Struers is a conductive bakelite resin with carbon filler embedding material), followed by grinding and polishing (last step: 1-μm diamond paste). A focused electron beam at an accelerating voltage of 15 kV and a current of 100 nA was applied. To obtain the element contents as a function of depth in the specimens, the intensities of the characteristic Ti-K$_\alpha$, Cr-K$_\alpha$, Fe-K$_\beta$, and N-K$_\alpha$ X-ray emission peaks were determined at points separated by 2 μm along lines perpendicular to the surface of the specimen in the specimen cross section. The concentrations of Ti, Cr, and Fe were determined based on the ratio of the concerned characteristic X-ray emission peak intensity of the specimen and that of a corresponding standard specimen (i.e., pure Ti, pure Cr, and pure Fe) by applying the $\Phi(\rho z)$-correction.[43]

To determine the characteristic X-ray emission peak of nitrogen, a correction procedure had to be applied because of severe overlap of the N-K$_\alpha$ and Ti-L$_l$ X-ray emission peaks. The correction procedure known as ratio method[44] was applied.

D. Transmission Electron Microscopy

TEM specimens were prepared as follows from 60 to 70 μm below the specimen surface in the nitrided zone.

Discs ($\Phi = 3$ mm) were stamped with a mechanical punch from sheets produced by removing material mechanically from both sides (faces) of a nitrided specimen. These discs were thinned to obtain an electron-transparent area, applying the jet-electropolishing technique with a Struers Tenupol-3 (Struers A/S, Ballerup,

Table I. The Contents of Cr, Ti and Light Element Impurities in the Alloy Specimens Before Nitriding

Element Alloy	Cr	Ti	N	O	S	C
	(at pct)			(μg/g)		
Fe-2 at pct Cr-2 at pct Ti	2.07 ± 0.01	2.00 ± 0.002	<10	11 ± 3	<10	10 ± 2

Table II. Summary of Applied Nitriding Parameters for the Fe-2 at pct Cr-2 at pct Ti Alloy

Alloy	Temp [K (°C)]	NH$_3$ (mL/min)	H$_2$ (mL/min)	r_N (atm$^{-1/2}$)	Time (h)	Specimen Code
Fe-2 at pct Cr-2 at pct Ti	833 (560)	25	475	0.054	1,3,12,20,24	LTHP
	833 (560)	2	498	0.004	6,12,24	LTLP
	853 (580)	2	498	0.004	6,12,18,24	HTLP

Denmark) apparatus (bath composition: 85 vol pct acetic acid and 15 vol pct perchloric acid, current: 24 mA ≤ I ≤ 42 mA, voltage: 19.5 V, temperature: 278 K (5 °C), flow rate setting: 20, and treatment time: 174 seconds ≤ t ≤ 242 seconds) and subsequently rinsed in ethanol, acetone, and isopropanol. To generate a hole in the middle of the sample, the discs were fixed between two platinum rings during the jet-electropolishing treatment.

TEM analysis was performed using a Philips CM 200 TEM operating at 200 kV. Bright-field (BF) and dark-field (DF) images as well as selected area diffraction patterns (SADPs) were taken employing a Gatan CCD camera (Gatan, Inc., Pleasanton, CA).

IV. RESULTS AND EVALUATION

A. Nitrogen Concentration Depth Profiles

The nitrogen concentration depth profiles of the Fe-2 at pct Cr-2 at pct specimens nitrided for LTHP, LTLP,

and HTLP have been determined by EPMA (Figure 1). An almost constant nitrogen level in the nitrided zone has been obtained for all specimens, except for the cases with relatively short nitriding time and with a low nitriding temperature, in which, in particular, the nitrogen concentration at the surface has not reached the "saturation" value observed upon prolonged nitriding. This outcome can be ascribed to the finite time needed to establish (near) local equilibrium (or a stationary state) at the specimen surface with the gas atmosphere (Section V).

B. Microstructural Analysis

TEM BF (top) and DF (middle) images and corresponding SADPs (insets) of nitrided Fe-2 at pct Cr-2 at pct alloy specimens (LTLP and HTLP) are shown in Figures 2(a) and (b). The electron-beam direction in both SADPs is close to (i.e., does not coincide exactly with) the [001] zone axis of the ferrite to avoid strong diffraction by the matrix and to reveal the presence of precipitates by their diffraction contrast.
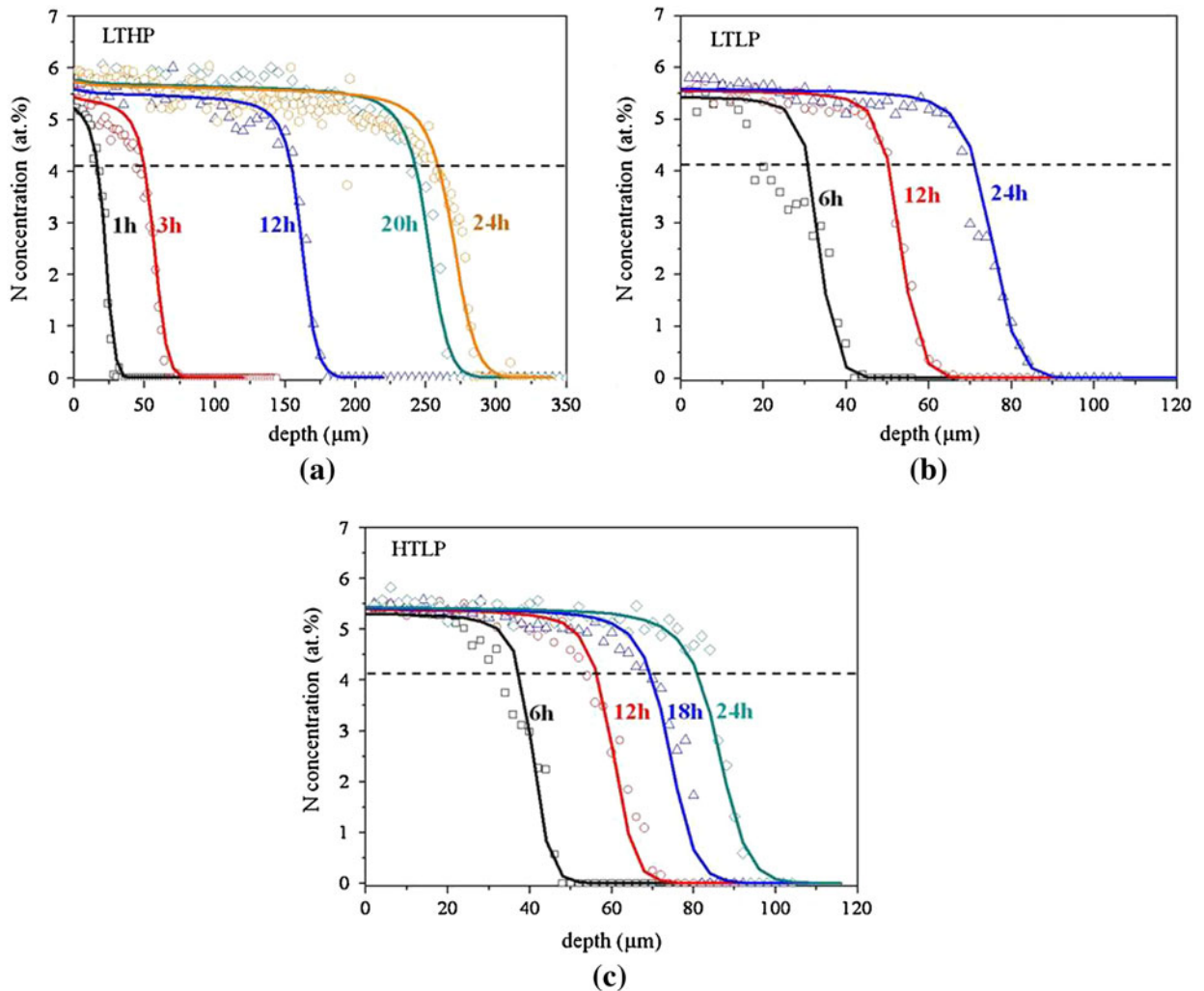

Fig. 1—Nitrogen concentration depth profiles determined by EPMA measurement (data points) and as determined by fitting of the numerical kinetic model for the case of mixed $Cr_{1-x}Ti_xN$ nitride precipitation (full lines). (a) LTHP, (b) LTLP, and (c) HTLP. The values obtained for the fit parameters are shown in Table III. The dashed lines indicate the so-called "normal nitrogen" content, which is the sum of the nitrogen incorporated in the stoichiometric nitrides and the equilibrium solubility of nitrogen in pure, unstrained ferrite matrix.
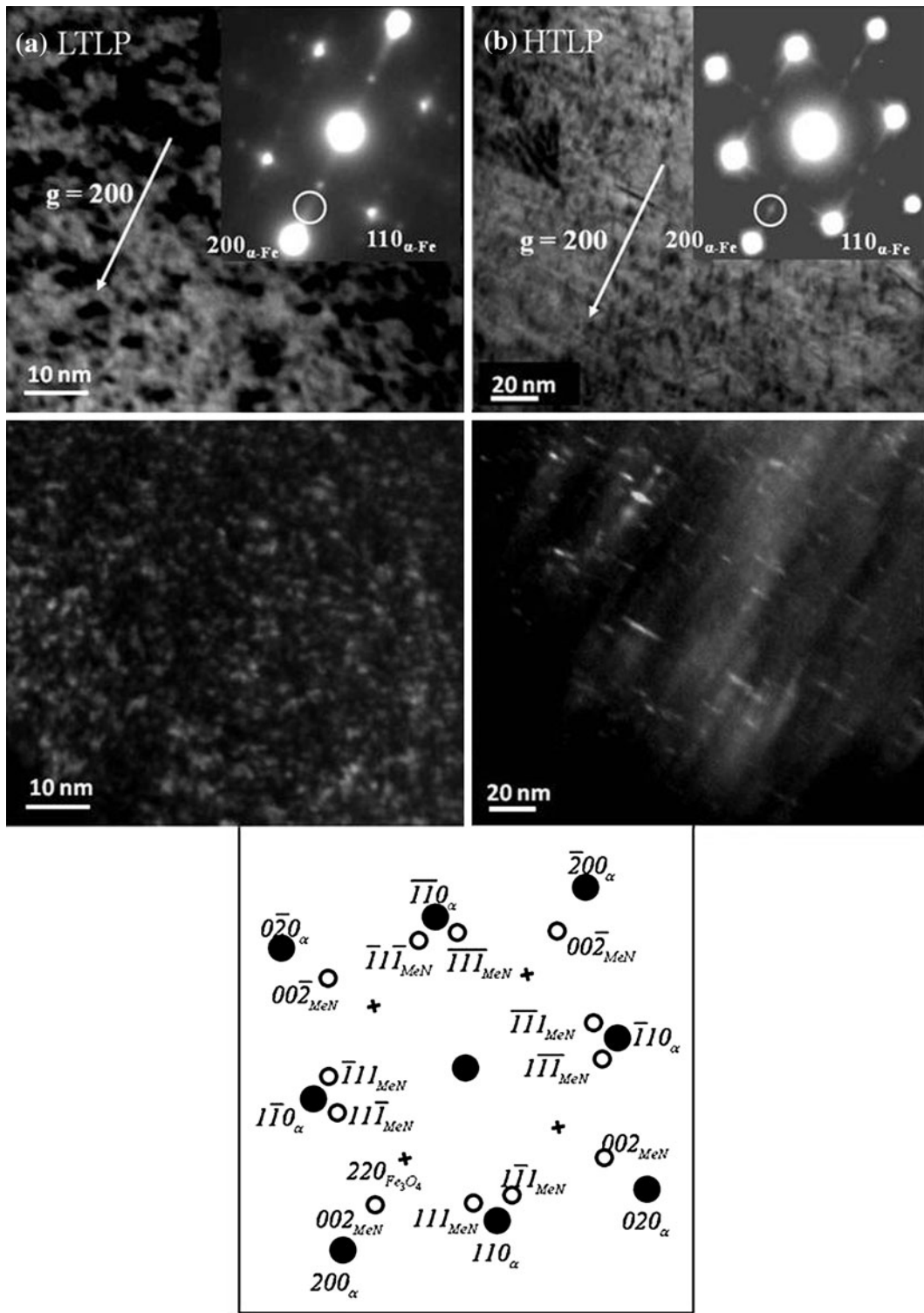
Fig. 2—TEM BF images (top), corresponding SADPs (insets), DF images (middle, as obtained from the streak and/or intensity maximum area selected by positioning the objective lens aperture at the position indicated by SADPs shown, for the concerned electron beam $[001]_{\alpha\text{-Fe}}$ direction and nitride precipitates complying with a Bain orientation relationship with the α-Fe matrix (black dots: diffraction spots of the ferrite matrix; unfilled circles: diffraction spots of the nitride precipitates). Fe-2 at pct Cr-2 at pct Ti alloys nitrided for 24 h with nitriding potential, $I_N = 0.004$ atm$^{-1/2}$ (TEM specimens are obtained about 60 to 70 μm below the specimen surface) for (a) LTLP and (b) HTLP.

In particular, for the LTLP specimen (Figure 2(a)), extremely fine nitride precipitates of hardly resolvable morphology can be discerned. For the HTLP specimen (Figure 2(b)), a relatively clear platelet-type morphology (length ≤20 nm and thickness ≤2 nm) of the nitride precipitates is observed. It follows that the size of the

nitride platelets increases (and the density of platelets decreases) with an increasing nitriding temperature at constant nitriding potential.

The SADPs recorded from all specimens show diffraction spots at locations corresponding to the ferrite matrix (the schematic diffraction patterns shown at the bottom in Figure 2). Additionally, streaks through the 200 and 020 type diffraction spots of the ferrite matrix can be observed. Furthermore, at a higher nitriding temperature, intensity maxima on these streaks occur at positions expected for 002 type spots of a cubic, rock salt, crystal structure–type nitride precipitate (Figure 2(b)).

The $200_{\alpha\text{-Fe}}$ diffraction spots in Figure 2(a) have split into two; one can be ascribed to cubic ferrite and the other one can be ascribed to tetragonally distorted ferrite. The tetragonal distortion is a consequence of the development of misfit strain between nitride precipitates and ferrite matrix. Similar observations have been made for nitrided binary Fe-V[45] with nitrides of rock salt crystal structure–type precipitate as platelets with $\{001\}_{\alpha\text{-Fe}}$ lattice planes and as habit planes. The mismatch of the nitride platelets with the ferrite matrix is such that, to maintain coherency, the ferrite matrix in the immediate surroundings of the nitride platelets is anisotropically tetragonally deformed; a compressive misfit stress develops in directions normal to the platelet (i.e., in a $<001>_{\alpha\text{-Fe}}$ direction), whereas a tensile misfit stress develops parallel to the platelet faces (i.e., in $<100/010>_{\alpha\text{-Fe}}$ directions). The surrounding ferrite matrix of the nitride platelet can thus be considered a body-centered tetragonal phase.[33,45]

If precipitates of CrN and TiN developed separately in the ferrite matrix during nitriding, then the diffraction spots of both nitrides should be distinguishable in the SADPs. However, the SADPs show only singular 111 reflections of a cubic rock salt crystal structure–type MeN nitride (note that the possible 002 spots lie on a streak [discussed earlier] and cannot be distinguished if separate spots would occur). This finding strongly suggests that Ti and Cr have precipitated together as a cubic rock salt–type mixed $Cr_{1-x}Ti_xN$ nitride (for extensive discussion of electron diffraction patterns recorded from nitrided alloys as investigated here, see Reference 33).

C. Numerical Modeling of Nitrogen Concentration Depth Profiles

Numerically calculated nitrogen concentration depth profiles, as described in Section II–B, were fitted to experimental data obtained by EPMA. The diffusion coefficient of nitrogen in the ferrite matrix, D_N is adopted as 8.7 μm²/s and 11.3 μm²/s at 833 K and 853 K (560 °C and 580 °C), respectively.[46] The fitting parameters are (1) the solubility products, $K_{Me_iN_n}$ or the solubility product, $K_{Me_{1,1-x}Me_{2,x}N_n}$, (2) the composition parameter, $n' = n + y$, and (3) the surface nitrogen concentration, $c^s_{N_\alpha}$ (cf. Section II).

A two-step fitting procedure for both of the two possible types of precipitation (separate nitrides or mixed nitride) has been applied.

For the precipitation of two separate nitrides, initial values of K_{CrN} and K_{TiN} have been adopted from Reference 35. After fitting the nitrogen concentration depth profiles for all the times at constant temperature separately, average values for K_{CrN} and K_{TiN} were obtained as (1) at 833 K (560 °C), $K_{CrN} = 0.03$ (atoms)²nm⁻⁶ and $K_{TiN} = 0.29 \times 10^{-15}$ (atoms)²nm⁻⁶ and (2) at 853 K (580 °C), $K_{CrN} = 0.05$ (atoms)²nm⁻⁶ and $K_{TiN} = 0.94 \times 10^{-15}$ (atoms)²nm⁻⁶, respectively. Note that, at constant temperature, the solubility products should not depend on nitriding potential and nitriding time. Furthermore, the composition parameters, n'_{CrN} or n'_{TiN} should also be independent of nitriding time, but they may depend on nitriding temperature and nitriding potential. From previous studies on nitrided iron-based binary Fe-Cr[15,34] and Fe-Ti[47,48] alloys, it follows that the amount of nitrogen adsorbed at the interface between the coherent CrN platelets and the ferrite matrix is small when compared with that of TiN in the ferrite matrix (i.e., $[N]^{CrN}_{imm,exc} < [N]^{TiN}_{imm,exc}$). Therefore, it can be assumed that the total amount of adsorbed nitrogen at the nitride platelet faces of the present nitrided Fe-Cr-Ti alloy is largely determined by n'_{TiN}. Therefore, in the fit procedure adopted here, the composition parameter of CrN, n'_{CrN}, was not considered as a fit parameter; its value was set equal to that determined in Reference 15—$n'_{CrN} = 1.12$. Thus, the aforementioned values of K_{CrN}, K_{TiN}, and n'_{CrN} were used as constants in the second definitive fitting, where only $c^s_{N_\alpha}$ and n'_{TiN} were considered as fit parameters.

For the precipitation of the mixed $Cr_{1-x}Ti_xN$ nitride, the nitrogen concentration depth profiles have been first fitted individually at each temperature (with $n'_{Cr_{1-x}Ti_xN}$, $c^s_{N_\alpha}$, and $K_{Cr_xTi_{1-x}N}$ as fit parameters). The averages of the determined values of $K_{Cr_xTi_{1-x}N}$ are $K_{Cr_xTi_{1-x}N} = 0.68 \times 10^{-3}$ (atoms)²nm⁻⁶ and $K_{Cr_xTi_{1-x}N} = 1.10 \times 10^{-3}$ (atoms)²nm⁻⁶ at 833 K (560 °C) and 853 K (580 °C), respectively. These values were then used as constants in the second, definitive fitting where only $c^s_{N_\alpha}$ and $n'_{Cr_{1-x}Ti_xN}$ were considered fit parameters.

First, the separate precipitation of CrN and TiN is considered. Using the procedure described earlier, the accordingly obtained best fit results for the measured nitrogen concentration depth profiles of the LTHP specimens nitrided for 12 hours and 20 hours are shown in Figures 3(a) and (b), respectively. A clear plateau region (denoted by arrows in Figure 3) can be discerned in the calculated nitrogen depth profiles (dashed lines). This finding can be interpreted as a direct consequence of a low value of K_{TiN} as compared with the value of K_{CrN} (discussed earlier); upon the arrival of dissolved nitrogen by diffusion, at a certain depth, it is consumed immediately by Ti to precipitate as TiN until the total local depletion of Ti has been realized. Only then can the dissolved Cr precipitate upon continued inward diffusion of nitrogen. As a consequence, only TiN precipitates develop at the nitriding front (i.e., the plateau region), whereas CrN precipitates develop in the zone closer to the surface where precipitation of TiN has been completed practically. Clearly, plateau regions in the nitrided zone adjacent to the case–core boundary do not occur in the experimental nitrogen concentration depth
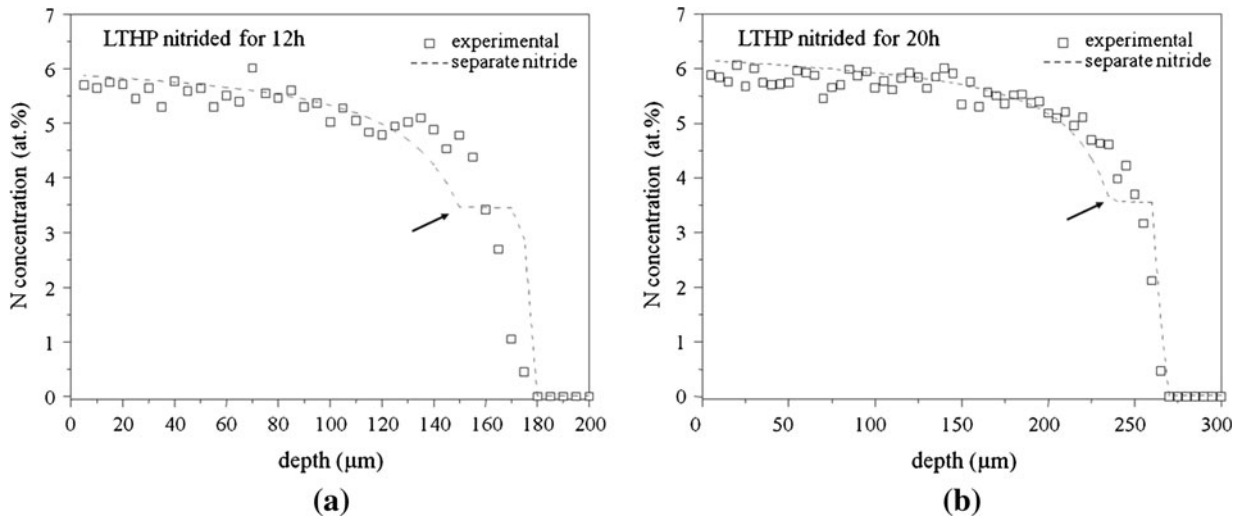
Fig. 3—Nitrogen concentration depth profiles determined by EPMA measurement (data points) and as determined by fitting to these data of the numerical kinetic model (dashed lines) for the precipitation of separate nitrides (TiN and CrN) for the LTHP specimens nitrided for (a) 12 h and (b) 20 h.

Table III.   Values Obtained for the Fit Parameters $K_{Cr_xTi_{1-x}N}$, $C^s_{N_\alpha}$ and $n'_{Cr_{1-x}Ti_xN}$

		Nitriding Time (h)						
Specimen		1	3	6	12	18	20	24
LTHP	$K_{Cr_xTi_{1-x}N}$ ((atoms)^{2}nm^{-6})	0.68×10^{-3}						
	$C^s_{N_\alpha}$ (at pct)	0.021	0.045	—	0.128	—	0.141	0.140
	$n'_{Cr_{1-x}Ti_xN}$	1.57	1.56	—	1.59	—	1.62	1.62
LTLP	$K_{Cr_xTi_{1-x}N}$ ((atoms)^{2}nm^{-6})	0.68×10^{-3}						
	$C^s_{N_\alpha}$ (at pct)	—	—	0.008	0.011	—	—	0.011
	$n'_{Cr_{1-x}Ti_xN}$	—	—	1.57	1.60	—	—	1.61
HTLP	$K_{Cr_xTi_{1-x}N}$ ((atoms)^{2}nm^{-6})	1.10×10^{-3}						
	$C^s_{N_\alpha}$ (at.%)	—	—	0.014	0.016	0.016	—	0.016
	$n'_{Cr_{1-x}Ti_xN}$	—	—	1.53	1.55	1.56	—	1.56

profiles. It has been concluded that separate precipitation of CrN and TiN is incompatible with the experimental data.

Second, the precipitation of a mixed nitrided, $Cr_{1-x}Ti_xN$ is considered. Using the corresponding fit procedure described earlier, the obtained best fit results for all specimens are shown in Figure 1 (full lines) together with the experimental data. The dashed lines in Figure 1 denote the normal nitrogen content, $[N]_{nor} = [N]_{MeN_n} + [N]^0_\alpha$. It follows that a large amount of excess nitrogen (the difference of $[N]_{tot}$ and $[N]_{nor}$) has been taken up (cf. Section II–A). The fitted and experimental nitrogen concentration depth profiles agree fairly well. The values obtained for the fit parameters—surface nitrogen concentration, $c^s_{N_\alpha}$, solubility product, $K_{Cr_xTi_{1-x}N}$, and the composition parameter, $n'_{Cr_{1-x}Ti_xN}$—are shown in Table III. The dependence of $c^s_{N_\alpha}$ as a function of nitriding time is shown in Figure 4, at constant temperature and at constant nitriding potential.

The experimentally determined values for $[N]_{tot}$ have an inaccuracy resulting in their presentation in at pct with only one decimal (see the EPMA data in Table IV).
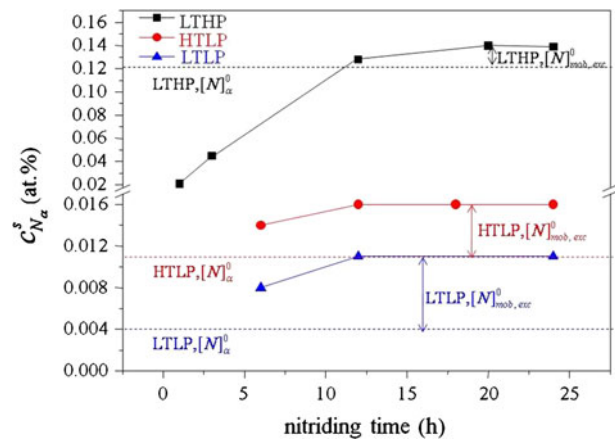

Fig. 4—The concentration of dissolved nitrogen at the surface of the specimen, $C^s_{N_\alpha}$, as a function of nitriding time. Results of fitting the numerical kinetic model for the case of mixed $Cr_{1-x}Ti_xN$ nitride precipitation (dashed lines indicate the equilibrium solubility of nitrogen in a pure, unstrained ferrite matrix, $[N]^0_\alpha$) for LTHP, LTLP, and HTLP specimens. The difference between $C^s_{N_\alpha}$ and $[N]^0_\alpha$ equals $[N]^0_{mob,exc}$.

Table IV. The Total Amount of Nitrogen at the Specimen Surface Determined by EPMA, $[N]^0_{tot,EPMA}$ (Taken as the Average Value of Five Data Points Near the Surface), and the Amounts $[N]^0_{tot,cal}$, $[N]^0_{mob,exc}$, and $[N]^0_{tmm,exc}$ at the Specimen Surface as Derived From the Fitted Kinetic Model for 24-Hour LTHP, LTLP, and HTLP Specimens

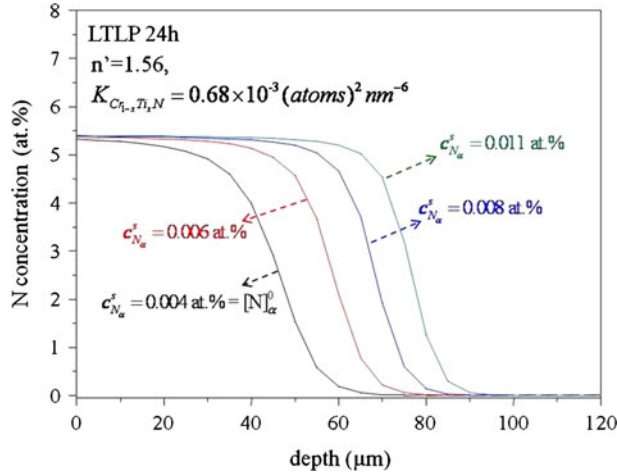| Specimen	$[N]^0_{tot,EPMA}$ (at pct)	$[N]^0_{tot,cal}$ (at pct)	$[N]^0_{mob,exc}$ (at pct)	$[N]^0_{tmm,exc}$ (at pct)
LTHP	5.9 ± 0.1	6.09	0.019	2.16
LTLP	5.8 ± 0.1	6.06	0.007	2.14
HTLP	5.6 ± 0.2	5.89	0.005	1.97

Fig. 5—Calculated nitrogen concentration depth profiles for a LTLP specimen as function of $C^s_{N_\alpha}$ (0.002 at pct) results in a significant nitrided depth difference (about 8 μm), which is experimentally well discernable.

The fitting of the nitrogen concentration depth profiles is highly sensitive to the values of $c^s_{N_\alpha}$, for example, the extent of the diffusion zone for a specimen nitrided under LTLP conditions increases about 8 μm by an $c^s_{N_\alpha}$ increase of only 0.002 at pct N (Figure 5). Therefore, the results in at pct for $c^s_{N_\alpha}$ and $[N]^0_{mob,exc}$ have been given with three decimals in Tables III and IV.

V. GENERAL DISCUSSION

During the nitriding of ferritic Fe-2 at pct Cr-2 at pct alloys, cubic, rock salt crystal structure–type mixed $Cr_{1-x}Ti_xN$ nitride platelets precipitate (Section IV–B). The formation of a mixed nitride seems to have even less of an obstacle for the nitriding of Fe-Cr-Ti alloy than for nitriding Fe-Cr-Al alloy[31]; both CrN[49] and TiN[50] have a cubic, rock salt–type equilibrium crystal structure, whereas AlN has an hexagonal, wurtzite-type equilibrium crystal structure.[20–23] Furthermore, uptake of Cr in TiN can be favored because it leads to a reduction of the misfit strain with the surrounding ferrite matrix.[33]

The surface concentration of dissolved nitrogen $c^s_{N_\alpha}$ increases with nitriding time until a saturation level has been reached (Figure 4). The initial increase of $c^s_{N_\alpha}$ is a consequence of the finite period of time necessary to establish local equilibrium, at the specimen surface, of the gas atmosphere with the solid substrate. This phenomenon has been observed for the nitriding of

pure iron and is a result of the competition of reactions of finite rate at the specimen surface, such as the dissociation of NH_3, the association of N atoms adsorbed at the specimen surface and their subsequent desorption as N_2 gas, and the diffusion of initially adsorbed and then dissolved nitrogen into the specimen; local equilibrium (instead of a stationary state) at the surface requires the desorption rate of nitrogen gas, formed by association of nitrogen atoms adsorbed at the surface, to be neglected.[42,51,52] The effect can be particularly strong in the presence of alloying elements that form nitrides because much more nitrogen has to be taken up before saturation, at the surface, can be attained. Note that at the shortest applied nitriding times, the values of $c^s_{N_\alpha}$ are even smaller than the equilibrium solubility of nitrogen in pure, unstrained ferrite (cf. dashed horizontal lines in Figure 4, which have been calculated according to Reference 42). After saturation, the amount of dissolved nitrogen at the surface has surpassed the equilibrium solubility in pure, unstrained ferrite, indicating the presence of mobile (i.e., dissolved) excess nitrogen. The values of $[N]^0_{mob,exc}$ can be calculated as $[N]^0_{mob,exc} = c^s_{N_\alpha} - [N]^0_\alpha$ (cf. Eq. [2]).

The presence of dissolved excess nitrogen in the ferrite matrix upon nitriding of Fe-Cr-Ti alloys is a consequence of elastic accommodation of the misfit between nitride platelet and ferrite matrix; such elastic accommodation of misfit induces a tensile hydrostatic stress component in the ferrite matrix.[53] As a consequence, compared with unstrained ferrite, more nitrogen can be dissolved (on octahedral interstices) in the ferrite matrix. The amount of dissolved nitrogen and, thus, $[N]^0_{mob,exc}$ in the ferrite matrix depends linearly on the nitriding potential.[53] Indeed, $[N]^0_{mob,exc}(LTHP) / [N]^0_{mob,exc}(LTLP) = 13.1$, which compares very well with $r_N (LTHP)/r_N (LTLP) = 13.1$. The size of the nitride precipitates increases with an increasing nitriding temperature (cf. results shown in Section IV–B). In general, upon coarsening, less misfit strain is accommodated elastically (beginning coherent $\rightarrow$ incoherent transition). As a consequence, the amount of $[N]^0_{mob,exc}$ decreases with increasing temperature, as observed (cf. results for LTLP and HTLP in Figure 4).

The largely coherent nature of the nitride platelet–matrix interface makes likely the adsorption of nitrogen at the octahedral interstices in the ferrite matrix adjacent to the platelet faces,[53] similar to how chemical bonding to Cr and/or Ti atoms in the platelet is realized (albeit, this chemical bonding is weaker than the nitrogen atoms within the nitride platelets). The presence of such immobile excess nitrogen (cf. Section II–A) is revealed by the values obtained for the nitride composition parameter, $n'_{Cr_{1-x}Ti_xN}$, which are distinctly larger than

one (*cf.* Table III). The amount of immobile excess nitrogen in the surface region (*i.e.*, for a fully precipitated stage and where equilibrium with the gas atmosphere has been realized), $[N]^0_{imm,exc}$, can be deduced from the value of the composition parameter, $n'_{Cr_{1-x}Ti_xN}$ and the amounts of alloying elements (*cf.* Table IV). Evidently, for the present nitriding conditions, $[N]^0_{imm,exc} >> [N]^0_{mob,exc}$.

It should be recognized that, although the amounts of mobile excess nitrogen are rather small, as compared with the amounts of immobile excess nitrogen, they have a great influence on the nitriding kinetics; the extent of the diffusion zone is significantly enhanced by these small amounts of nitride excess nitrogen (Figure 5). Indeed, $[N]^0_{mob,exc}$ is not small compared with $[N]^0_\alpha$ (*cf.* Figure 4).

As compared with the LTLP results, the somewhat lower amount of $[N]^0_{imm,exc}$ of HTLP (*cf.* Table IV) is compatible with the larger platelet thickness and, thus, results in a lesser amount of nitride–matrix interface, as observed by TEM (*cf.* Section IV–B). Accordingly, the thickness of the precipitates can be estimated using the following equation[30]:

$$\text{Thickness} = \frac{2}{\left(n'_{Cr_{1-x}Ti_xN} - 1 \right)} \times \frac{a_{Cr_{1-x}Ti_xN}}{2} \qquad [9]$$

where $a_{Cr_{1-x}Ti_xN}$ is the lattice parameter of the mixed nitride. Assuming that the lattice parameter of the mixed $Cr_{1-x}Ti_xN$ nitride complies with Vegard's law and using literature values for the lattice parameters of CrN and TiN (0.414 nm for rock salt crystal structure–type CrN[49] and 0.424 nm for rock salt crystal structure–type TiN[50]), the lattice parameter of mixed Cr1 – xTixN nitride with $x = 0.49$ is $a_{Cr_{1-x}Ti_xN} = 0.419$ nm. Using this lattice parameter value and the experimental values of $n'_{Cr_{1-x}Ti_xN}$ (1.62, 1.61, and 1.56 for LTHP, LTLP, and HTLP, respectively), the thickness of the nitride platelet is obtained as 0.68, 0.69, and 0.75 nm for LTHP, LTLP, and HTLP, respectively. The larger value for the nitride platelet thickness of the HTLP specimens is compatible with the TEM analysis presented in Section IV–B.

VI. CONCLUSIONS

1. Upon the nitriding of ternary iron-based ferritic Fe-Cr-Ti alloys, highly coherent cubic, rock salt, crystal structure–type, mixed $Cr_{1-x}Ti_xN$ nitrides develop as platelets (thickness <2 nm) in the ferrite matrix obeying a Bain orientation relationship with the ferrite matrix, with $\{100\}_{\alpha\text{-Fe}}$ habit planes. The platelets are surrounded by a tetragonally distorted ferrite matrix.
2. A numerical model developed to describe the nitriding kinetics of ternary iron-based Fe-Me$_1$-Me$_2$ alloys leads to agreement with the experimentally determined nitrogen concentration depth profiles provided the separate roles of mobile excess nitrogen (dissolved in the ferrite matrix) and immobile excess nitrogen (adsorbed at the nitride-platelet–matrix

interface) are recognized. The results obtained are compatible with the precipitation of the mixed $Cr_{1-x}Ti_xN$ nitride, and not of separate CrN and TiN nitrides, which is in agreement with the TEM data.
3. The surface concentration of dissolved nitrogen increases with nitriding time until a saturation level is attained as a consequence of the strong affinity of, in particular, Ti for N as well as the competition of the diffusion rate of dissolved nitrogen, the rate of ammonia dissociation at the surface, and the rate of desorption of adsorbed nitrogen as nitrogen gas from the surface.
4. For a given degree of nitride-platelet–matrix coherency, the amount of mobile excess nitrogen primarily depends on the nitriding potential, whereas the amount of immobile excess nitrogen primarily depends on the size of the precipitates (*i.e.*, the interface density).
5. The amount of immobile (adsorbed) excess nitrogen is much larger than the amount of mobile (dissolved) excess nitrogen. Yet, the relatively tiny amount of mobile excess nitrogen is responsible for a district increase of the depth of the nitrided zone. The immobile excess nitrogen appreciably enhances the nitrogen level of the nitrided zone.

REFERENCES

1. S. Lampman: *ASM Handbook*, vol. 4, ASM International, Materials Park, OH, 1991, pp. 259–67.
2. H. Ferkel, M. Glatzer, Y. Estrin, R.Z. Valiev, C. Blawert, and B.L. Mordike: *Mater. Sci. Eng. A*, 2003, vol. A348, pp. 100–10.
3. M. Pellizzari, A. Molinari, and G. Straffelini: *Mater. Sci. Eng. A*, 2003, vol. A352, pp. 186–94.
4. N. Limodin and Y. Verreman: *Mater. Sci. Eng. A*, 2006, vols. A435–436, pp. 460–67.
5. A. Basu, J.D. Majumdar, S.G. Chowdhury, P.K. Ajikumar, P. Shankar, A.K. Tyagi, B. Raj, and I. Manna: *Surf. Coat. Technol.*, 2007, vol. 201, pp. 6985–92.
6. T. Hirsch, T.G.R. Clarke, and A. da Silva Rocha: *Surf. Coat. Technol.*, 2007, vol. 201, pp. 6380–86.
7. S. Jegou, L. Barrallier, and R. Kubler: *Acta Mater.*, 2010, vol. 58, pp. 2666–76.
8. G. Miyamoto, A. Yonemoto, Y. Tanaka, T. Furuhara, and T. Maki: *Acta Mater.*, 2006, vol. 54, pp. 4771–79.
9. G. Miyamoto, A. Yonemoto, Y. Tanaka, T. Maki, and T. Furuhara: *ISIJ Int.*, 2009, vol. 49, pp. 1801–05.
10. B. Mortimer, P. Grieveson, and K.H. Jack: *Scand. J. Metall.*, 1972, vol. 1, pp. 203–09.
11. K.H. Jack: *Proc. Heat Treatment Conf. London, 1973*, TMS, London, UK, 1975, pp. 39–50.
12. B.J. Lightfoot and D.H. Jack: *Proc. Heat Treatment Conf. London 1973*, TMS, London, UK, 1975, pp. 59–65.
13. R.E.E. Pulkkinen: *Scand. J. Metall.*, 1983, vol. 12, pp. 87–92.

14. R.E. Schacherl, P.C.J. Graat, and E.J. Mittemeijer: *Z. Metallkd.*, 2002, vol. 93, pp. 468–77.
15. R.E. Schacherl, P.C.J. Graat, and E.J. Mittemeijer: *Metall. Mater. Trans. A*, 2004, vol. 35A, pp. 3387–98.
16. S.S. Hosmani, R.E. Schacherl, and E.J. Mittemeijer: *Mater. Sci. Technol.*, 2005, vol. 21, pp. 113–24.
17. S.S. Hosmani, R.E. Schacherl, and E.J. Mittemeijer: *J. Mater. Sci.*, 2008, vol. 43, pp. 2618–24.
18. S.S. Hosmani, R.E. Schacherl, L.L. Dobrzyńska, and E.J. Mittemeijer: *Phil. Mag.*, 2008, vol. 88, pp. 2411–26.
19. H.H. Podgurski, R.A. Oriani, and F.N. Davis: *Trans. TMS-AIME*, 1969, vol. 245, p. 1603.
20. H.H. Podgurski and H.E. Knechtel: *Trans. TMS-AIME*, 1969, vol. 245, pp. 1595–1602.
21. M.H. Biglari, C.M. Brakman, M.A.J. Somers, W.G. Sloof, E.J. Mittemeijer, and S. Van Der Zwaag: *Z. Metallkd.*, 1993, vol. 84, pp. 124–31.
22. M.H. Biglari, C.M. Brakman, E.J. Mittemeijer, and S. Van Der Zwaag: *Phil. Mag. A*, 1995, vol. 72, pp. 1281–99.
23. M.H. Biglari, C.M. Brakman, E.J. Mittemeijer, and S. Van Der Zwaag: *Phil. Mag. A*, 1995, vol. 72, pp. 931–47.
24. H.J. Spies, H. Biermann, and A. Fischer: *Z. Metallkd.*, 2005, vol. 96, pp. 781–86.
25. W.D. Welch and S.H. Carpenter: *Acta Metall.*, 1973, vol. 21, pp. 1169–79.
26. M. Pope, P. Grieveson, and K.H. Jack: *Scand. J. Metall.*, 1973, vol. 2, pp. 29–34.
27. A. Krawitz: *Scripta Metall.*, 1977, vol. 11, pp. 117–22.
28. M.M. Yang and A.D. Krawitz: *Metall. Trans. A*, 1984, vol. 15A, pp. 1545–54.
29. S.S. Hosmani, R.E. Schacherl, and E.J. Mittemeijer: *Acta Mater.*, 2005, vol. 53, pp. 2069–79.
30. S.S. Hosmani, R.E. Schacherl, and E.J. Mittemeijer: *Acta Mater.*, 2006, vol. 54, pp. 2783–92.
31. A.R. Clauss, E. Bischoff, R.E. Schacherl, and E.J. Mittemeijer: *Metall. Mater. Trans. A*, 2009, vol. 40A, pp. 1923–34.
32. K.S. Jung, R.E. Schacherl, E. Bischoff, and E.J. Mittemeijer: *Surf. Coat. Technol.*, 2010, vol. 204, pp. 1942–46.
33. K.S. Jung, R.E. Schacherl, E. Bischoff, and E.J. Mittemeijer: *HTM J. Heat Treatm. Mat.*, 2010, vol. 65, pp. 237–42.
34. P.M. Hekker, H.C.F. Rozendaal, and E.J. Mittemeijer: *J. Mater. Sci.*, 1985, vol. 20, pp. 718–29.
35. Y. Sun and T. Bell: *Mater. Sci. Eng. A*, 1997, vol. A224, pp. 33–47.
36. J.D. Kamminga and G.C.A.M. Janssen: *Surf. Coat. Technol.*, 2005, vol. 200, pp. 909–12.
37. J.D. Kamminga and G.C.A.M. Janssen: *Surf. Coat. Technol.*, 2006, vol. 200, pp. 5896–5901.
38. K. Bongartz, D.F. Lupton, and H. Schuster: *Metall. Trans. A*, 1980, vol. 11A, pp. 1883–93.
39. K. Bongartz, W.J. Quadakkers, R. Schulten, and H. Nickel: *Metall. Trans. A*, 1989, vol. 20A, pp. 1021–28.
40. J. Crank: *The Mathematics of Diffusion*, Clarendon Press, Oxford, UK, 1970.
41. E.J. Mittemeijer and J.T. Slycke: *Surf. Eng.*, 1996, vol. 12, pp. 152–62.
42. E.J. Mittemeijer and M.A.J. Somers: *Surf. Eng.*, 1997, vol. 13, pp. 483–97.
43. J.L. Pouchou and F. Pichoir: *Rech. Aerosp.*, 1984, pp. 167–92.
44. A. Armigliato, L. Dori, A. Garulli, and P. Venturi: *J. Microsc. Spectrosc. Electron.*, 1982, vol. 7, pp. 593–603.
45. N.E. Vives Diaz, S.S. Hosmani, R.E. Schacherl, and E.J. Mittemeijer: *Acta Mater.*, 2008, vol. 56, pp. 4137–49.
46. J.D. Fast and M.B. Verrijp: *J. Iron Steel Inst.*, 1954, vol. 126, pp. 24–27.
47. D.S. Rickerby, S. Henderson, A. Hendry, and K.H. Jack: *Acta Metall.*, 1986, vol. 34, pp. 1687–99.
48. D.H. Kirkwood, O.E. Atasoy, and S.R. Keown: *Met. Sci.*, 1974, vol. 8, pp. 49–55.
49. M. Nasr Eddine, E.F. Bertaut, and M. Maunaye: *Acta Cryst.*, 1977, vol. B33, pp. 2696–98.
50. W. Lengauer, S. Binder, K. Aigner, P. Ettmayer, A. Guillou, J. Debuigne, and G. Groboth: *J. Alloys. Compd.*, 1995, vol. 217, pp. 137–47.
51. H.C.F. Rozendaal, E.J. Mittemeijer, P.F. Colijn, and P.J. Van Der Schaaf: *Metall. Trans. A*, 1983, vol. 14A, pp. 395–99.
52. P.B. Friehling, F.W. Poulsen, and M.A.J. Somers: *Z. Metallkd.*, 2001, vol. 92, pp. 589–95.
53. M.A.J. Somers, R.M. Lankreijer, and E.J. Mittemeijer: *Phil. Mag. A*, 1989, vol. 59, pp. 353–78.